

Smooth Triaxial Weaving with Naturally Curved Ribbons

Changyeob Baek,^{1,2} Alison G. Martin³, Samuel Poincloux², Tian Chen^{2,4} and Pedro M. Reis^{2,*}¹*Department of Mechanical Engineering, Massachusetts Institute of Technology, Cambridge, Massachusetts 02139, USA*²*Flexible Structures Laboratory, Institute of Mechanical Engineering, École Polytechnique Fédérale de Lausanne (EPFL), Lausanne 1015, Switzerland*³*Fivizzano, Italy*⁴*Computer Graphics and Geometry Laboratory, School of Computer and Communication Sciences, École Polytechnique Fédérale de Lausanne (EPFL), Lausanne 1015, Switzerland* (Received 24 November 2020; revised 9 July 2021; accepted 12 July 2021; published 31 August 2021)

Triaxial weaving is a handicraft technique that has long been used to create curved structures using initially straight and flat ribbons. Weavers typically introduce discrete topological defects to produce nonzero Gaussian curvature, albeit with faceted surfaces. We demonstrate that, by tuning the in-plane curvature of the ribbons, the integrated Gaussian curvature of the weave can be varied continuously, which is not feasible using traditional techniques. Further, we reveal that the shape of the physical unit cells is dictated solely by the in-plane geometry of the ribbons, not elasticity. Finally, we leverage the geometry-driven nature of triaxial weaving to design a set of ribbon profiles to weave smooth spherical, ellipsoidal, and toroidal structures.

DOI: 10.1103/PhysRevLett.127.104301

Traditional basketmakers have long been employing the handicraft technique of triaxial weaving to fabricate intricate shell-like structures by interweaving initially straight ribbons into tridirectional arrays [1,2]. Beyond basketry, triaxial weaving is also encountered in textiles [3], composite materials [4], molecular chemistry [5,6], and biology [7]. While weaving with straight ribbons in a regular hexagonal pattern yields a flat surface, topological defects (e.g., pentagons or heptagons) induce local out-of-plane geometry [1,8–10]. Basketmakers have extensive empirical know-how on how and where to place these defects, and recent research has investigated their optimal placements to approximate target surfaces [2,11]. The strategy to achieve shape by defects is also akin to the concept of topological charge [12] in curved two-dimensional (2D) crystals such as the buckminsterfullerene [13], colloidal crystals [14–16], confined elastic membranes [17,18], and dimples on curved elastic bilayers [19,20]. However, the curvature attained from these defects is discrete, which limits the range of realizable shapes. Even if previous studies [21,22] have suggested a polygon-based combinatorial design procedure that includes weaving with initially curved ribbons, a predictive understanding of the effect of the ribbon geometry on the shape of the weave is lacking.

Here, we investigate how triaxial weaving with naturally curved (in-plane) ribbons can yield smooth three-dimensional (3D) shapes. We make use of a combination of rapid prototyping, x-ray microcomputed tomography (μ CT), and finite element methods (FEMs) to perform a detailed characterization of the geometry of our woven structures. First, we take a unit-cell approach to

systematically explore how the original 2D geometry of the ribbons dictates the 3D shape of the weaves and regard these cells as building blocks to construct more complex woven objects. Figure 1 and the associated video in the Supplemental Material [23] show representative unit cells with different topological characteristics and with ribbons with different in-plane curvatures. Excellent agreement is found between the experiments (μ CT) and simulations (FEM). These unit cells comprise n identical ribbons that are woven to form an n -gon surrounded by a total of n triangles. Each ribbon has three segments (indexed by

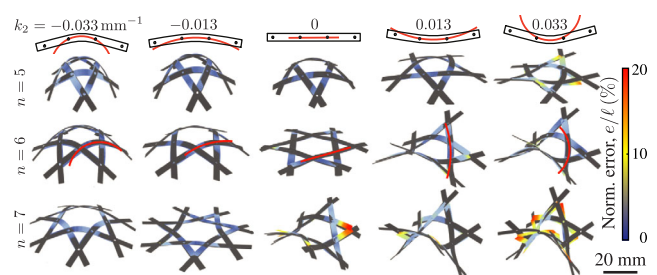


FIG. 1. Representative family of triaxially woven unit cells for different numbers of ribbons (rows, $n = \{5, 6, 7\}$) and for different values of the in-plane curvature in their middle segment (columns, $k_2 = \{-0.033, -0.013, 0, 0.013, 0.033\} \text{ mm}^{-1}$). All ribbons have three segments, each of arc length $\ell_1 = \ell_2 = \ell_3 = 15 \text{ mm}$; only the middle one is curved ($k_2 \neq 0 \text{ mm}^{-1}$), while those in the two extremities are naturally flat ($k_1 = k_3 = 0 \text{ mm}^{-1}$). Tomographic μ CT scans (gray images) are juxtaposed on FEM simulations, color coded by the distance between their respective centerlines locations e/ℓ . See the associated video in the Supplemental Material [23].

$j = \{1, 2, 3\}$), with rivets placed at the crossing points to fix the segment length ℓ_j . The in-plane curvature k_j of each segment can be varied continuously (see red solid lines in Fig. 1). Traditional weaving corresponds to the case of straight ribbons, $k_j = 0 \text{ mm}^{-1}$ (Fig. 1, middle column). By considering ribbons that are naturally curved in plane (examples in Fig. 1 with $k_2 \neq 0$), we demonstrated that the curvature of the resulting surface of the unit cells can be tuned smoothly, in a way not possible through the traditional approach. A purely geometric analysis is performed to rationalize the integrated Gaussian curvature of the physical unit cells, revealing that geometry is at the core of setting the shape of our physical triaxial weaves. This geometric reasoning forms the basis of a set of design principles, which are then leveraged to construct a variety of smooth canonical structures, including spherical, ellipsoidal, and toroidal weaves.

Before turning to the general case of curved ribbons, we first focus on the “traditional weaving” of unit cells with naturally *straight* ribbons ($k_1^\circ = k_2^\circ = k_3^\circ = 0$); hereon, the superscript $(\cdot)^\circ$ denotes quantities pertaining to straight ribbons. In Fig. 2(a), we present the photograph of a physical unit cell for a representative case with $n = 5$ ribbons. The specimens were fabricated by, first, laser cutting ribbons of width 4 mm from a polymer sheet and, then, hand weaving them to produce a 3D structure, which was imaged tomographically using a μ CT scanner (μ CT100, Scanco Medical; $a = 29.3 \mu\text{m}$ voxel size). The original polymer sheet was a bilayer of a polyethylene terephthalate (PETE; Young’s modulus $E_1 \approx 3 \text{ GPa}$) plate

of thickness $t_1 = 0.25 \text{ mm}$, coated with an elastomer-metal composite ($E_2 \approx 1 \text{ MPa}$) of thickness $t_2 = 0.35 \text{ mm}$. The latter comprised vinylpolysiloxane (VPS-16, Zhermack) infused with a metal powder (NdFeB, 30065-089, neo Magnequench; $\approx 5 \mu\text{m}$ particle size) mixed at 2–1 weight ratio. Given the disparity in bending stiffnesses of the two layers, $E_1(t_1)^3/[E_2(t_2)^3] \approx \mathcal{O}(10^3)$, the mechanical stiffness of the ribbons was provided by the PETE, with a width-to-thickness ratio of 16. The radiopacity of the elastomer-metal served in detecting the ribbons using x-ray tomography to extract their framed centerlines from the volumetric data ([23], Sec. 1) [Fig. 2(b)]. The corresponding framed centerlines extracted from FEMs (see [23], Sec. 2.1 for procedure) are in excellent agreement with the experiments, as demonstrated in Fig. 2(c).

We characterize the shape of the unit cells by quantifying their curvature. However, since the n -gon in the woven unit cell does not possess a well-defined surface (its inner region is void of material), it is impossible to define a pointwise Gaussian curvature K . However, the n -gon does have a well-defined boundary, set by the ribbons centerlines. We define the *integrated* Gauss curvature of the unit cell, $\mathcal{K}_n = \int_A K dA$, where A is a surface enclosed by and tangent to the centerlines of the n -gon [for example, the shaded region in Fig. 2(b)]. The remarkable Gauss-Bonnet theorem [26] states that \mathcal{K}_n is independent of the embedding of the surface A , and it can be determined directly by quantifying the n -gon boundary

$$\mathcal{K}_n = (2 - n)\pi - \sum_{i=1}^n \kappa_g^i + \sum_{i=1}^n \theta^i, \quad (1)$$

where $\kappa_g^i = \int_i k_g ds$ is the integrated geodesic curvature of the i th edge and θ^i is the i th interior angle of the n -gon at each crossings [see schematic definitions in Fig. 2(b)]. \mathcal{K}_n is the key quantity that we investigate throughout this study. Toward evaluating \mathcal{K}_n , as presented in Fig. 2(d), we first measured experimental and simulated averages of both the integrated geodesic curvature $\langle \kappa_g^\circ \rangle = 1/n \sum_{i=1}^n \kappa_g^i$ and the interior angles $\langle \theta^\circ \rangle = 1/n \sum_{i=1}^n \theta^i$ for representative unit cells with $3 \leq n \leq 9$. Within the same cell, we find that all ribbons share the same values of κ_g^i and θ^i (their standard deviation is smaller than the symbol size), as expected from rotational symmetry. In the region $n \geq 5$, $\langle \theta^\circ \rangle \approx 2\pi/3$ independent of n , indicating that the exterior triangles remain developable and the Gaussian curvature concentrates at the n -gon ([23], Sec. 2.2). To rationalize this observation, we use geometrical arguments based on either a spherical or a conical underlying geometry to estimate the bending energy of the unit cells ([23], Sec. 2.3), showing that it is a decreasing function of n . Therefore, it is energetically more favorable to bend an n -gon with $n > 3$ than the external triangles, which can be regarded as nearly developable. However, our current understanding does not draw a full picture of the intricate coupling

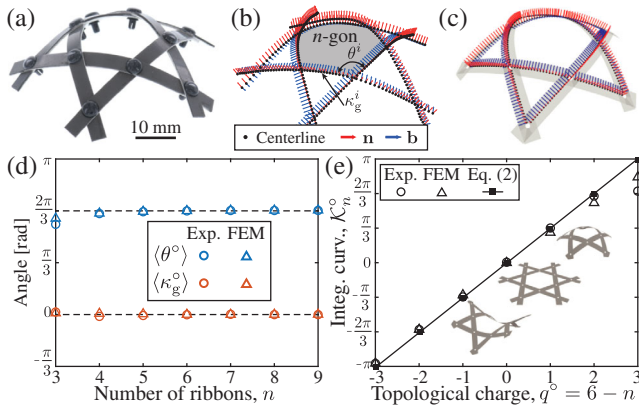


FIG. 2. Unit cells woven with straight ribbons. (a) Photograph of a unit cell with $n = 5$ straight ribbons. (b) Experimental data of the framed centerlines of the cell in (a) extracted from μ CT ([23], Secs. 1.1–3). (c) FEM-computed version of (b). (d) Average interior angles of the n -gon $\langle \theta^\circ \rangle$ and average integrated geodesic curvatures $\langle \kappa_g^\circ \rangle$ vs n . The horizontal dashed lines at $\langle \theta^\circ \rangle = 2\pi/3$ and $\langle \kappa_g^\circ \rangle = 0$ are drawn to aid visual comparison with the geometric prediction. (e) Integrated Gaussian curvature of the unit cells with straight ribbons \mathcal{K}_n , computed through Eq. (1), vs $q^\circ = 6 - n$. The solid line is the prediction from Eq. (2). Inset: FEM-computed unit cells with $q^\circ = \{-3, -2, \dots, 3\}$, or equivalently $n = \{9, 8, \dots, 3\}$.

between elasticity and geometry in these woven structures, whose structural rigidity remains an open problem. Moreover, the vanishing integrated geodesic curvature $\langle \kappa_g^\circ \rangle \approx 0$ is a direct consequence of the mechanics of elastic ribbons; ribbons favor out-of-plane (instead of in-plane) deformation [27]. Combining these observations with Eq. (1), we arrive at the expression for the integrated Gauss curvature of a unit cell with straight ribbons,

$$\mathcal{K}_n^\circ = \frac{\pi}{3}(6 - n), \quad (2)$$

where the integer $q^\circ = 6 - n$ is analogous to the topological charge in curved crystallography [12]. From the measurements on the n -gon boundary presented in Fig. 2(d), we compute \mathcal{K}_n° as a function of q° , as shown in Fig. 2(e), onto which we superpose the predictions from Eq. (2) and FEM computations for unit cells with $q^\circ = \{-3, -2, \dots, 3\}$, corresponding to $n = \{9, 8, \dots, 3\}$. Despite some discrepancies for $n \leq 4$, Eq. (2) describes both the experimental and FEM results well. Equation (2) demonstrates that the discrete nature of q° constrains strongly the possible shapes of the unit cells in traditional weaving [1,2].

Next, we come back to the nontraditional case of weaving unit cells with naturally curved ribbons, representative examples of which were presented in Fig. 1. In Fig. 3(a), we show schematic diagrams of an individual curved ribbon (top), as well as the planar representation of the corresponding unit cell (bottom). Note that, although the schematic is drawn planar in Fig. 3(a), the woven unit cells are, in general, nonplanar. Each segment with $j = \{1, 2, 3\}$ is color coded as red, green, and blue, respectively. We seek to evaluate the effect of the initial in-plane curvature k_j on the integrated curvature of the cell \mathcal{K}_n as a function of n . For convenience, we normalize the segment curvature by its arc length: $\kappa_j = k_j \ell_j$. The $(2\pi/n)$ -fold rotational symmetry is ensured naturally by the definition of the unit cell when n is even and enforced when n is odd by further imposing $\ell_1 = \ell_3$ and $\kappa_1 = \kappa_3$. This dense sampling is sufficient to quantify the effect of the in-plane geometry of the ribbons. Motivated by our findings for unit cells with straight ribbons [Fig. 2(d)], we make the following remarks. First, we assume that the ribbons keep their in-plane curvature when woven; hence, $\kappa_j^\circ = \int_j k_j ds = \int_j k_j ds = k_j \ell_j = \kappa_j$ for every segment of the n -gon [27]. Second, for straight ribbons, we found that the outer triangles remained isometric, thereby enclosing a surface of vanishing integrated curvature; a statement that we now assume to remain valid for unit cells woven with curved ribbons. Leveraging this assumption on the outer triangles, we evaluate the interior angles of the triangles [opposite to the arc ℓ_j ; see Fig. 3(a)] using Euclidean trigonometry: $\phi_j = \cos^{-1}(\sum_{m \neq j} (g_m^2 - g_j^2)/2 \prod_{m \neq j} g_m) - \sum_{m \neq j} \kappa_m/2$, where $g_j = 2 \sin(\kappa_j/2) \cdot \ell_j/\kappa_j$. In turn, the interior angles of the n -gon θ^i are the supplementary angle

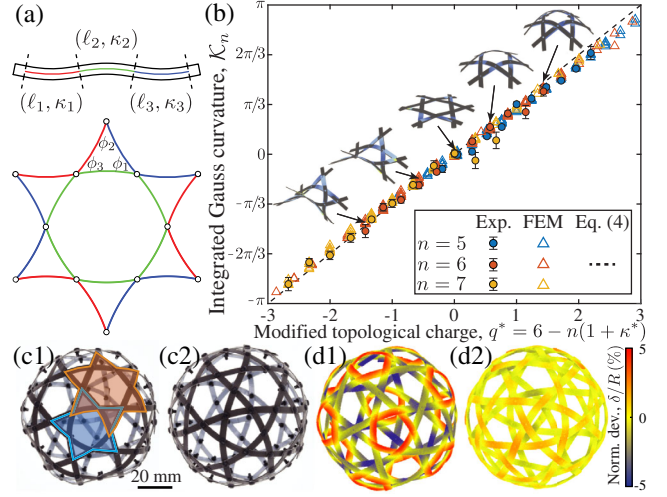


FIG. 3. Weaving with curved ribbons. (a) Schematics of the ribbons (top) and the planar representation of a typical unit cell. The ribbons have three distinct curved segments of arc length ℓ_j and normalized curvature κ_j ($j = 1, 2, 3$; color coded as red, green, and blue, respectively). (b) Integrated Gaussian curvature of the unit cells vs $q^* = 6 - n(1 + \kappa^*)$, with κ^* from Eq. (3). Inset: unit cells with $n = 6$, $\kappa_1 = \kappa_3 = 0$, and from left to right $\kappa_2 = \{0.5, 0.2, 0, -0.2, -0.5\}$. (c1),(c2) Photographs of spherical weaves with (c1) straight and (c2) curved ribbons. The weaves consist of 12 pentagonal (blue shaded region) and 20 hexagonal (orange shaded region) unit cells. (d1),(d2) Reconstructed μ CT images of the weaves in (c1) and (c2), respectively. The color bar indicates the normalized voxelwise radial deviation δ/R from a sphere of radius $R = 42$ mm.

of either ϕ_1 or ϕ_3 , such that $\sum_{i=1}^n \theta^i = \{n(\pi - \phi_1) + n(\pi - \phi_3)\}/2$. Thus, using the Gauss-Bonnet theorem stated in Eq. (1), the integrated curvature of a unit cell reads $\mathcal{K}_n = \pi/3[6 - n(f + \kappa^*)]$, where $f = 3/2\pi \cos^{-1}(g_2^2 - g_1^2 - g_3^2/2g_1g_3)$, and

$$\kappa^* = \frac{3}{4\pi}(-\kappa_1 + 2\kappa_2 - \kappa_3). \quad (3)$$

The arc length ℓ_j and the curvature κ_j are coupled through the nonlinear term f . Noting that $g_j \approx \ell_j$ in the range of in-plane curvatures considered, $|\kappa_j| \leq 0.5$ [e.g., $g_j(\kappa_j = 0.5) \approx 0.99\ell_j$], we take the asymptotic limit of $|\kappa_j| \ll 1$. We further impose $\ell_1 = \ell_2 = \ell_3$ to quantify only the effect of the in-plane curvatures. Ultimately, we obtain $f = 1$ and Gauss-Bonnet reduces to

$$\mathcal{K}_n(\kappa_1, \kappa_2, \kappa_3) = \frac{\pi}{3}[6 - n(1 + \kappa^*)]. \quad (4)$$

From the similitude between Eqs. (4) and (2), we define $q^* = 6 - n(1 + \kappa^*)$ as the “modified topological charge” of the unit cell with *curved* ribbons. We highlight that q^* can be varied smoothly using curved ribbons, yielding a continuous range of \mathcal{K}_n , whereas \mathcal{K}_n° in Eq. (2) was discrete and restricted to multiples of $\pi/3$.

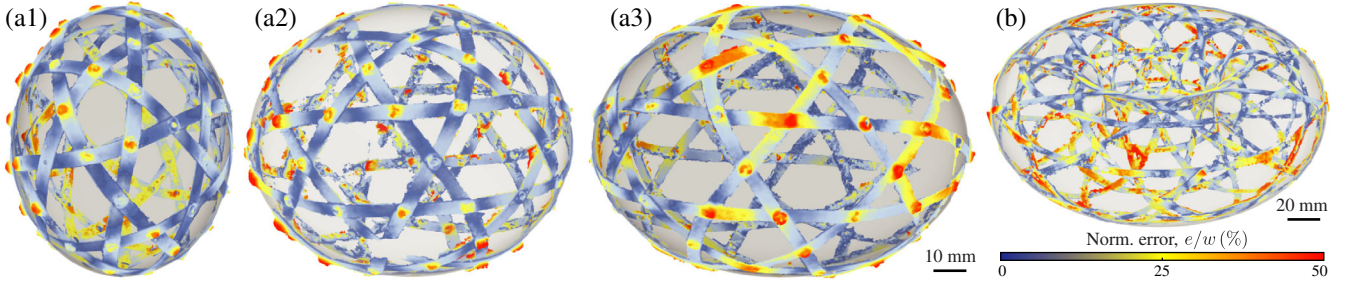


FIG. 4. Nonspherical weaves with initially curved ribbons, reconstructed by photogrammetry. The color bar indicates the normalized deviation from a target surface e/w , where w is the ribbon width. (a1)–(a3) Ellipsoidal weaves of aspect ratios, $a/b = \{0.75, 1.25, 1.5\}$, respectively. (b) Toroidal weave of inner radius $r_i = 35$ mm and outer radius $r_o = 105$ mm. The planar geometries of the underlying curved ribbons for each of these weaves are provided in the Supplemental Material ([23], Secs. 3.2–3.3)

In Fig. 3(b), we plot experimental and FEM data for \mathcal{K}_n vs q^* , while fixing $\ell_j = 15$ mm, to systematically explore the parameter space $n = \{5, 6, 7\}$ and $\kappa_2 = \{-0.5, \dots, 0.5\}$ (in steps of 0.1). Also, the experiments had $\kappa_1 = \kappa_3 = 0$ (total of 33 configurations, with two experiments per configuration) and the simulations had $\kappa_1 = \pm\kappa_3 = \{-0.5, -0.2, 0, 0.2, 0.5\}$ (total of 352 configurations). To convey the change of shape associated with variations of the integrated curvature, we also juxtapose the unit cells with $n = 6$ and varying ribbon curvatures that we presented in Fig. 1. As above for the unit cells with straight ribbons, we measured θ^i and κ_g^i of the n -gon and used Eq. (1) to compute \mathcal{K}_n ([23], Sec. 1.3). Remarkably, we find that the data in Fig. 3 collapse over the full range of $-\pi \leq \mathcal{K}_n \leq \pi$. This continuous variation for curved ribbons is in contrast to the analogous result for traditional weaving [Fig. 2(e)], where \mathcal{K}_n^c was limited to discrete steps of $\pi/3$ [cf. Fig. 2(e)]. Importantly, our geometric prediction for \mathcal{K}_n from Eq. (4) is in excellent agreement with the data, demonstrating that in-plane ribbon geometry is at the heart of our triaxial weaving problem.

Thus far, we followed a unit-cell approach to demonstrate that smooth weaving can be physically realized with curved ribbons, purely from geometric design principles. We now seek to assemble these unit cells into a spherical weave, adopting the topology of the “rectified truncated icosahedron” [28,29] for the layout of our design. We fix the segment length to $\ell_s = 15$ mm and inject a (nondimensional) segment curvature $\kappa_s = k_s \ell_s$ into the pentagonal cells. The resulting weave comprises 12 pentagonal cells with $(\kappa_1, \kappa_2, \kappa_3) = (0, \kappa_s, 0)$ and 20 hexagonal cells with $(\kappa_1, \kappa_2, \kappa_3) = (\kappa_s, 0, 0)$, marked with blue and orange shaded regions in Fig. 3(c1), respectively. In Figs. 3(c1) and 3(c2), we present photographs of two spherical weaves: one with straight ribbons ($\kappa_s = 0$), the traditional case, and the other with curved ribbons ($\kappa_s = 0.3$). The corresponding μ CT images are shown in Figs. 3(d1) and 3(d2), color coded by the radial distance between the scans and a sphere of radius $R = 42$ mm, δ (mm). Negative values of δ indicate voxels located inside the targeted sphere. For the weave with straight ribbons [Fig. 3(d1)], the pentagons

protrude from the reference sphere, with 5% maximum radial deviation. This faceted geometry is a signature of the localized curvature intrinsic to the discrete nature of traditional weaving; Eq. (4) predicts $\mathcal{K}_5 = \pi/3$ for the pentagons and $\mathcal{K}_6 = 0$ for the hexagons. By contrast, the weave with curved ribbons ($\kappa_s = 0.3$) shown in Fig. 3(d2) exhibits a significantly smoother shape, with a radial deviation within 1% of the perfect sphere; Eq. (4) predicts $\mathcal{K}_5 = 0.3$ and $\mathcal{K}_6 = 0.45$.

Our unit cells with curved ribbons are rotationally symmetric. Hence, the possible design space available by their tessellation is limited to shapes with local symmetry [e.g., the sphere in Fig. 3(c)]. We do not expect this approach to be, in general, viable to design weaves with more complex or arbitrary geometries. To overcome this limitation, we expanded our framework to design the initial shape of piecewise-circular ribbons that are to be woven into a given target surface. Similar to what we did for the unit cells, the injection of geodesic curvature into the weave through the in-plane curvature of the ribbons is at the core of the procedure. Our design protocol (detailed in [23], Sec. 3.1) consists of inputting a target surface, onto which we project a graph representing the triaxial weave topology. This graph contains “nodes” (corresponding to the crossing points of the ribbons) and “edges” for their connectivity. At each node, a geodesic turning angle between consecutive nodes is computed with respect to the target surface. The shape of piecewise-circular segments of the ribbon is then obtained by averaging the two geodesic turning angles from its neighboring crossing points.

In Figs. 4(a1)–4(a3), as the first example of nonspherical designs, we present reconstructed images of ellipsoidal weaves of an equatorial radius $b = 40$ mm and polar radii $a = \{30, 50, 60\}$ (mm). The graph for these weaves was obtained by adopting the topology of the rectified truncated icosahedron [28,29] and linearly expanding it by a factor a along the x, y axes and a factor b along the z axis ([23], Sec. 3.2). Photogrammetry was used to reconstruct the 3D shape of the ellipsoidal woven structures from a series of photos with different perspectives ([23], Sec. 1.4). The

reconstructed meshes are color coded with errors from their target surface normalized by their ribbon width, $w = 4$ mm. Even though our design strategy did not incorporate the elastic energy of the ribbons, excellent agreement is found between the target surfaces and the weaves, exhibiting the distance error smaller than 50% of the ribbon width. In an ellipsoid, only the meridians and the equator are the closed geodesics [26], it is not trivial to achieve smooth oblate [Fig. 4(a1)] and prolate [Figs. 4(a2) and 4(a3)] ellipsoidal weaves. Curved ribbons enable one to accommodate variations of the aspect ratio of the ellipsoids, while keeping the same weave topology. As a second example, a smooth torus (genus-zero surface with zero total curvature [26]) cannot be achieved through traditional weaving; using straight ribbons inevitably requires the placement of pentagonal and hexagonal defects, albeit with a localization of curvature that leads to faceted geometry. By contrast, as demonstrated by the physical realization in Fig. 4(b), our design with curved ribbons yields a toroidal weave with hexagonal cells alone, the in-plane curvature of the ribbons distributing the total curvature. The presented smooth toroidal weave has an inner radius $r_i = 35$ mm and an outer radius $r_o = 105$ mm. The topology of the toroidal weave was obtained by mapping a regular triaxial pattern in a 2D parameter space to a 3D toroidal target surface ([23], Sec. 3.3).

The planar layout of the curved ribbons used in the above designs (spherical, ellipsoidal, and toroidal) are provided in the Supplemental Material [23] and can be cut and woven by the interested reader.

Our Letter demonstrates that the discrete nature of traditional triaxial weaving can be circumvented by using initially curved piecewise-circular ribbons. The shape of the weaves can be decoupled from their topology, with multiple topological layouts and ribbons geometries leading to the same woven shapes. However, when woven, these geometrically identical solutions store elastic energy differently [[23], S2.1]. This observation calls for a full optimization problem, which we hope future work will address, where both the distance from the target surface and the associated elastic energy are minimized in tandem by changing the geodesic curvatures and the segment lengths of the ribbon as design parameters. Beyond art and architecture, future implementations of our design framework may include morphing structures in which the in-plane curvature of ribbons would be preprogrammed into the ribbons and actuated upon stimuli to attain desired target shapes.

We thank Yingying Ren, Julian Panetta, Florin Isvoranu, Christopher Brandt, and Mark Pauly for fruitful discussions.

Note added in the proof.—After submission of our manuscript, the following study [30] on weaving of arbitrary

geometries has been published, using the mechanism uncovered in the present study at the core of their design principle.

*Corresponding author.

pedro.reis@epfl.ch

- [1] A. G. Martin, in *Proceedings of IASS Annual Symposia* (International Association for Shell and Spatial Structures (IASS), Madrid, 2015), Vol. 2015, pp. 1–8.
- [2] P. Ayres, A. G. Martin, and M. Zwierzycki, in *Advances in Architectural Geometry 2018* (Klein Publishing GmbH (Ltd), Vienna, 2018), pp. 72–93.
- [3] N. F. Dow and G. Tranfield, *Text. Res. J.* **40**, 986 (1970).
- [4] A. S. Phani and N. A. Fleck, *J. Appl. Mech.* **75**, 021020 (2008).
- [5] U. Lewandowska, W. Zajaczkowski, S. Corra, J. Tanabe, R. Borrmann, E. M. Benetti, S. Stappert, K. Watanabe, N. A. Ochs, R. Schaeublin *et al.*, *Nat. Chem.* **9**, 1068 (2017).
- [6] Y. Liu, M. O’Keeffe, M. M. Treacy, and O. M. Yaghi, *Chem. Soc. Rev.* **47**, 4642 (2018).
- [7] F. M. Brodsky, C.-Y. Chen, C. Knuehl, M. C. Towler, and D. E. Wakeham, *Annu. Rev. Cell Dev. Biol.* **17**, 517 (2001).
- [8] J.-F. Sadoc and R. Mosseri, *Geometrical Frustration* (Cambridge University Press, Cambridge, England, 2006).
- [9] D. S. Richeson, *Euler’s Gem: The Polyhedron Formula and the Birth of Topology* (Princeton University Press, Princeton, NJ, 2012).
- [10] S. J. Callens and A. A. Zadpoor, *Mater. Today* **21**, 241 (2018).
- [11] J. Vekhter, J. Zhuo, L. F. G. Fandino, Q. Huang, and E. Vouga, *ACM Trans. Graph.* **38**, 1 (2019).
- [12] D. R. Nelson, *Phys. Rev. B* **28**, 5515 (1983).
- [13] H. W. Kroto, J. R. Heath, S. C. O’Brien, R. F. Curl, and R. E. Smalley, *Nature (London)* **318**, 162 (1985).
- [14] A. Dinsmore, M. F. Hsu, M. Nikolaidis, M. Marquez, A. Bausch, and D. Weitz, *Science* **298**, 1006 (2002).
- [15] A. Bausch, M. J. Bowick, A. Cacciuto, A. Dinsmore, M. Hsu, D. Nelson, M. Nikolaidis, A. Travesset, and D. Weitz, *Science* **299**, 1716 (2003).
- [16] W. T. Irvine, V. Vitelli, and P. M. Chaikin, *Nature (London)* **468**, 947 (2010).
- [17] H. S. Seung and D. R. Nelson, *Phys. Rev. A* **38**, 1005 (1988).
- [18] G. M. Grason and B. Davidovitch, *Proc. Natl. Acad. Sci. U.S.A.* **110**, 12893 (2013).
- [19] M. Brojan, D. Terwagne, R. Lagrange, and P. M. Reis, *Proc. Natl. Acad. Sci. U.S.A.* **112**, 14 (2015).
- [20] F. L. Jiménez, N. Stoop, R. Lagrange, J. Dunkel, and P. M. Reis, *Phys. Rev. Lett.* **116**, 104301 (2016).
- [21] J. Mallos, in *Proceedings of ISAMA* (The International Society of the Arts, Mathematics, and Architecture, Albany, 2009), pp. 13–19, <http://www.isama.org/hyperseeing/09/09b.pdf>.
- [22] E. Akleman, J. Chen, Q. Xing, and J. L. Gross, *ACM Trans. Graph.* **28**, 1 (2009).
- [23] See Supplemental Material at <http://link.aps.org/supplemental/10.1103/PhysRevLett.127.104301> for animated version of Fig. 1, details on volumetric data analysis, FEM simulations and procedure to weave ellipsoids and torus, which includes Refs. [24,25]. We also provide the layout of the strips for the spherical, ellipsoidal, and toroidal weaves,

- which can be directly printed and cut manually or with a laser cutter.
- [24] A. I. Bobenko, J. M. Sullivan, P. Schröder, and G. Ziegler, *Discrete Differential Geometry* (Springer, New York, 2008), Vol. 38.
- [25] M. Bergou, M. Wardetzky, S. Robinson, B. Audoly, and E. Grinspun, *ACM Trans. Graph.* **27**, 1 (2008).
- [26] J. J. Stoker, *Differential Geometry* (John Wiley & Sons, New York, 1969).
- [27] M. A. Dias and B. Audoly, *J. Elast.* **119**, 49 (2015).
- [28] D. Barbaro, in *Biblioteca di architettura urbanistica* (A. Forni, Sala Bolognese, 1980), p. 97.
- [29] C. S. Kaplan and G. W. Hart, in *Bridges: Mathematical Connections in Art, Music, and Science*, edited by R. Sarhangi and S. Jablan (Winfield, 2001), pp. 21–28; available online at <http://archive.bridgesmathart.org/2001/bridges2001-21.html>.
- [30] Y. Ren, J. Panetta, T. Chen, F. Isvoranu, S. Poincloux, C. Brandt, A. Martin, and M. Pauly, *ACM Trans. Graph.* **40**, 1 (2021).